ORIGINAL PAPER



Application of the double-difference relocation method to acoustic emission events in high-pressure deformation experiments

Timothy Officer¹ · Lupei Zhu² · Ziyu Li² · Tony Yu¹ · David R. Edey³ · Yanbin Wang¹

Received: 26 January 2022 / Accepted: 24 May 2022 © The Author(s), under exclusive licence to Springer-Verlag GmbH Germany, part of Springer Nature 2022

Abstract

A methodology has been developed, detailing the theory and workflow, for applying the double-difference relocation method to acoustic emission (AE) event location in high-pressure/high-temperature deformation experiments in the multi-anvil apparatus. The process is predicated on the fact that events originating from a common source region will traverse similar ray paths from the source to the receiver and display similar waveforms in seismograms. This implies their travel-time difference results only from their spatial offset and any velocity heterogeneity along the ray path is negated. To demonstrate the efficacy of this approach we applied it to a transformational faulting experiment on the isostructural olivine analogue Mg₂GeO₄ under controlled deformation at 2.5 GPa and 700 °C while simultaneously monitoring stress, strain, and acoustic activity. Waveforms from all 1456 AE events were cross-correlated to measure differential arrival times and construct multiplet groups of similar events. In total, 110 multiplets were identified whose size is dominated by two large groups containing 272 and 202 events. Relocation of these two multiplets using the double-difference method significantly reduces event separation and improves location uncertainty by more than an order of magnitude when compared to absolute location techniques whose uncertainty rivals that of the sample size. In particular, event locations of the two largest multiplets reveal two dense clusters whose spatial geometry closely mirrors that of macroscopic faulting displayed in computerized tomography images of the recovered sample. In this way, we are able to link specific faults with their associated AE events, which would otherwise not be possible using traditional absolute location methods.

 $\textbf{Keywords} \ \ Deep-focus \ earthquakes \cdot Transformational \ faulting \cdot Multi-anvil \ apparatus \cdot Earthquake \ location \cdot Double-difference \ method$

Introduction

One of the major unresolved questions in earth science involves the mechanism(s) by which earthquakes can nucleate, initiate and propagate under high pressure/high

This article is part of a Topical Collection "Experimental & Analytical Techniques at Extreme & Ambient Conditions", guest edited by Stella Chariton, Vitali B. Prakapenka and Haozhe (Arthur)

☐ Timothy Officer officer@cars.uchicago.edu

Published online: 06 July 2022

- Center for Advanced Radiation Sources, The University of Chicago, Chicago, IL, USA
- Department of Earth and Atmospheric Sciences, Saint Louis University, St. Louis, MO, USA
- Jackson School of Geosciences, University of Texas at Austin, Austin, TX, USA

temperature (HPHT) conditions more than > 60 km below the surface. This is due to the fact that brittle failure is strongly inhibited by high confining pressure which prevents crack growth. Furthermore, the elevated temperature at these depths promotes creep and flow, suggesting plastic yielding should occur before the fracture stress is reached. Nevertheless, deep-focus earthquakes (i.e., earthquakes that occur at depths below ~ 300 km) are observed routinely in the cold lithospheric cores of subduction zones (Frohlich 2006). For several decades since their discovery (Wadati 1927), progress in this area was slow due to a lack of experimental confirmation associated with the difficulty of running experiments under in situ conditions of HPHT. However, over the past several years, advances in high-pressure technology have permitted a growing number of investigations that are able to address this problem directly by performing HPHT mineral deformation experiments in multi-anvil apparatuses coupled with acoustic emission (AE) monitoring. The addition of



sonic information is significant considering it provides realtime information about the sample's mechanical behavior in situ. This knowledge can be exploited to elucidate meaningful information regarding the dynamics of the rupture process. However, the multi-anvil apparatus is inherently noisy and generates spurious signals that need to be discriminated from meaningful AEs that originate within the sample. By employing an array of piezoelectric sensors surrounding the high-pressure assembly and invoking seismological techniques commonly used for earthquake location, AE events can be located. In most cases, this has been accomplished through inverting P-wave arrival times using a homogeneous velocity model (e.g. de Ronde et al. 2007; Schubnel et al. 2013; Ohuchi et al. 2018; Officer and Secco 2020). However, this approach is limited by two major sources of uncertainty. First, errors in arrival times, usually obtained by automatic picking, lead directly to uncertainty in absolute location. Second, the assumption of velocity homogeneity is, in reality, never achieved in the multi-anvil apparatus since the P-waves originating in the sample pass through several mechanically distinct materials between source and receiver. This leads to reflections, refraction, and scattering resulting in inaccurate travel time estimates which further impacts location estimates. Taken together these sources of uncertainty generally result in location errors on the order of mm. Given the intrinsic limitations placed on sample volume in high-pressure generation, samples are typically restricted to only a few mm in size. Consequently, location uncertainties tend to be on the order of the sample size. Therefore, to draw robust conclusions about AE origin within the sample necessitates sub-mm accuracy in event location. Furthermore, this precludes the possibility of understanding how clusters of densely spaced similar events develop since the spatial extent of such clusters may be below the resolution of location. Such information is critical when attempting to assess the processes by which microfractures interact and coalesce to generate macroscopic failure. One method to reduce location uncertainty is the double-difference relocation method, which relies on differential arrival times, as opposed to absolute arrival times, to locate seismic events relative to one another. Over the years, this technique has been applied successfully to earthquake seismology (e.g. Got et al. 1994; Waldhauser and Ellsworth 2000) and adapted for hydraulic fracturing (e.g. Arrowsmith and Eisner 2006; Castellanos and van der Baan 2013). More recently, this technique was employed successfully to AE experiments in the multi-anvil apparatus demonstrating a significant reduction in location uncertainty (Wang et al. 2017; Shi et al. 2018).

In this study, we applied the double-difference method to determine relative AE event locations using HPHT AE waveform data. We adopted the hypoDD code developed by Waldhaser and Ellsworth (2000). We modified the code so that it can use a Cartesian coordinate system directly without

the need to transform the geographic coordinate system in the original code, and the sensors can be located anywhere in a whole space. The purpose of this paper is to generate a methodology that can be put into practice by the HPHT AE community to determine event locations more accurately within the sample. This process first requires cross-correlation of waveforms to measure accurate differential arrival times. Then hypoDD is applied to the data to determine highly accurate relative event locations for events in different clusters. By doing so we were able to achieve more than an order of magnitude improvement in event location accuracy compared to locations determined using traditional arrival time inversions.

Double-difference method: theory and workflow

The double-difference method relies on the fact that two (or more) events, whose spatial separation is much smaller than both heterogeneities in velocity and the event-sensor distance, will traverse similar ray paths from the source to a common receiver. Therefore, the travel-time difference to a common sensor results only from the spatial offset of the events since the effects of velocity heterogeneities along the ray path will cancel out. Consequently, only the velocity in the vicinity of the source is relevant. This is especially true for highly similar events that originate in dense clusters with limited spatial extent. For this reason, it is essential that accurate differential arrival times are measured.

The double-difference algorithm: hypoDD

Under the assumption of a constant velocity model, the arrival time of an AE event i, that occurred at time τ^i and location x^i, y^i, z^i , at sensor k can be expressed as:

$$t_k^i = \frac{1}{v} \left[\left(x^i - x_k \right)^2 + \left(y^i - y_k \right)^2 + \left(z^i - z_k \right)^2 \right]^{1/2} + \tau^i \tag{1}$$

In most instances, locations of events in HPHT experiments have been calculated using the earthquake location method of Geiger (1912) (e.g. de Ronde et al. 2007), which linearizes Eq. (1) by applying a truncated Taylor series expansion to form the equation,

$$\frac{\partial t_k^i}{\partial \mathbf{m}} \Delta \mathbf{m}^i = d_k^i \tag{2}$$

where $d_k^i = (t^{\text{obs}} - t^{\text{cal}})_k^i$ is the difference between the observed, t^{obs} , and theoretically calculated, t^{cal} , arrival times, and $\Delta \mathbf{m}^i = (\Delta x^i, \Delta y^i, \Delta z^i, \Delta \tau^i)$. Equation (2) relates perturbations in the hypocenter, $\Delta \mathbf{m}^i$, to travel-time residuals d_k^i for event i at the kth sensor and is only appropriate for measured



29

arrival times. In contrast, the hypoDD algorithm uses arrival time differences between events to calculate their relative hypocenter locations and origin times (Waldhauser and Ellsworth 2000). From Eq. (2), the arrival time difference of events *i* and *j* form the equation,

$$\frac{\partial t_k^{ij}}{\partial \mathbf{m}} \Delta \mathbf{m}^{ij} = \Delta d_k^{ij} \tag{3}$$

where $\Delta \mathbf{m}^{ij} = (\Delta x^{ij}, \Delta y^{ij}, \Delta z^{ij}, \Delta \tau^{ij})$, represents the change in the relative location parameters between events *i* and *j*.

$$\Delta d_k^{ij} = (t_k^i - t_k^j)^{\text{obs}} - (t_k^i - t_k^j)^{\text{cal}}$$
 (4)

is called the double-difference arrival time since it is the difference between the observed and calculated *differential* arrival time between the event pair. It is important to note that Eq. (4) only requires differential arrival times between events i and j, and therefore can use measured arrival times of individual events or differential arrival times between events as inputs. By combining all event pairs for each station, and amalgamating every station, Eq. (3) can be written in matrix form as:

$$WG\Delta m = W\Delta d \tag{5}$$

G is a matrix of size $M \times 4 N$ (M is the number of double-difference observations and N is the number of events), that is populated by the partial derivatives $\partial t_k^{ij}/\partial \mathbf{m}$; $\Delta \mathbf{m}$ is a vector of length 4N containing the event parameters we wish to determine, namely Δx , Δy , Δz , and $\Delta \tau$; $\Delta \mathbf{d}$ is a vector of size M containing the double-difference arrival time for each event pair, and W is a diagonal matrix introduced to weight each equation. Equation (5) can then be solved in a least-squares sense,

$$\Delta m = \left(G^{\mathrm{T}} W^{-1} G\right)^{-1} G^{\mathrm{T}} W^{-1} \Delta d \tag{6}$$

In practice, Eq. (5) is solved as follows: starting with an initial estimate of the event parameters, $m_{\text{initial}} = (x, y, z, \tau)_{\text{initial}}$, the entries of the partial derivative matrix G and the double-difference arrival time Δd are calculated and used to solve the system of linear equations and Δm is computed using Eq. (6). The solution is updated to $m_{\text{new}} = m_{\text{intial}} + \Delta m$ and the process is repeated in an iterative fashion starting with m_{new} as the new m_{intial} . The process is continued until stopping criteria are met such as the change in the solution is below a certain threshold or the maximum number of iterations is reached.

Event waveform cross-correlation

AE events are generated by rapid adjustment of the localized stress field and can occur anywhere within the sample, however, they tend to accompany fault formation and slip. In particular, events associated with specific faults

will tend towards similar rupture processes (Geller and Mueller 1980: Arrowsmith and Eisner 2006). Because such events arise from similar processes, they also tend to possess similar source mechanisms and originate within close proximity to one another. This, in turn, leads to similar waveforms in seismograms recorded by a common sensor. By employing cross-correlation of waveforms, we are able to identify similar events originating from a common source region. Two similar events are termed a "doublet" if their maximum cross-correlation coefficient is greater than a pre-defined value. A group of more than two similar events is termed a multiplet. Following the approach used by Arrowsmith and Eisner (2006), we define multiplets as a cluster of n events (n > 2) where each event forms a doublet with at least one other event in the multiplet. In this way, multiplets are constructed in a chain-like manner as opposed to the stricter definition that enforces all events in a multiplet to be mutually correlated with all other events (De Meersman et al. 2009). While imposing that all events in a multiplet correlate with one another can be useful in rejecting poorly linked events, it precludes the possiblity of monitoring subtle systematic changes that occur in time or space that may reveal important information regarding the physics of the source. The practice of classifying clusters of events into multiplets has several advantages. Identifying events with similar origins allows for high precision relative locations of events which can help verify the presence and geometry of faults otherwise not resolvable using less accurate location techniques (Wang et al. 2017). It also has the ability to recognize the reactivation of a fault.

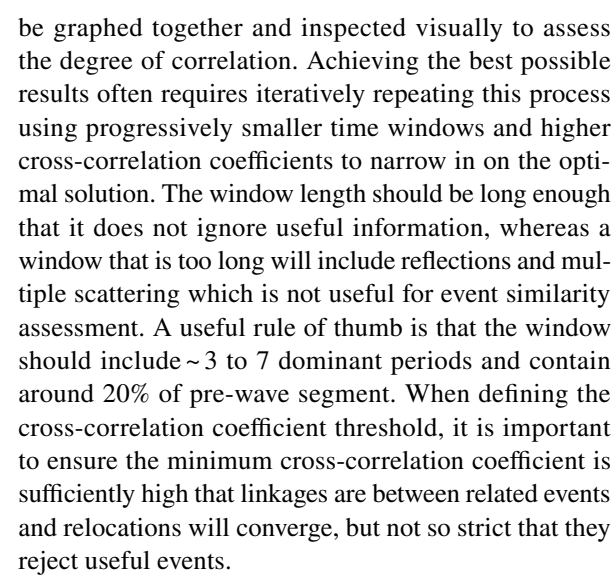
In addition to multiplet identification, the use of waveform cross-correlation provides an additional benefit. Because hypoDD relies on relative arrival times, instead of absolute arrival times, we are able to take advantage of cross-correlation to accurately determine relative P-wave arrival times, using the lag time of the maximum crosscorrelation coefficient. This procedure can be automated, provided the onsets of the P-waves lie within the correlation time window. Although this process can be computationally expensive for large numbers of waveforms, it requires comparatively little effort on behalf of the operator since they need only define the cross-correlation time window and coefficient threshold. This can save a tremendous amount of time over manual refinement of arrival time picks. A further benefit of using this method is that relative arrival times need not have the phase arrival positions at the exact onset of the P-wave impulse since correlated waveforms will be shifted from the true phase arrival by the same duration. This is especially useful for waveforms with less impulsive P-waves which hinder manual inspection and automatic picking algorithms.



Workflow

The procedure for computing event locations using hypoDD can be broken into five main stages: (1) initial estimation of arrival times, (2) measure differential arrival times using waveform cross-correlation and compute maximum cross-correlation coefficients for event pairs, (3) run hypoDD to define multiplets and compute relative locations of event-sto take advantage of cross-correlation to accuratelywithin each multiplet, (4) assess the results to determine if previous stages require improvement, and (5) constrain the absolute locations of events by anchoring a single position within each multiplet to its corresponding absolute location.

- 1. Initial arrival time estimation: Prior to carrying out differential arrival time refinement, an initial estimate of absolute P-arrival times must be made for every waveform included in the analysis. At this stage the arrival times need not be exact, however, it is advantageous to approximate the arrival times as close to the "true" value as possible. In particular, they need to be close enough to the true arrival times that the phase arrival is contained within the window used when running cross-correlation. The simplest approach is to set all the arrival times to a value based on a priori knowledge of the waveforms, for example, the threshold crossing time, however, this can be fairly inaccurate. Another relatively expedient way to estimate arrival times is to use an automatic picking algorithm (e.g. Akaike information criterion (AIC) method (Akaike 1974); RMS amplitude method; Short Time Average over Long Time Average (STA/LTA) method (Allen 1982); the wavelet method (Anant and Dowla 1997); autoregressive method (Sleeman and van Eck 1999), etc.). Recent developments in machine learning-based phase picking may also prove useful for this purpose (e.g. Ross et al. 2018; Mousavi et al. 2020; Cano et al. 2021; Saad et al. 2021; Li et al. 2022). Manual picking can also be used and is generally more effective than automatic methods, but far more time consuming. Regardless of what method is used for the initial arrival time estimates, it is useful to plot the waveforms and verify that the phase arrivals, at the very least, are confined to the dimensions of the correlation window. Those that do not should be adjusted until they do, or the correlation window needs to be widened.
- 2. Measure differential arrival times using waveform cross-correlation: Once the initial arrival times have been estimated, waveforms collected on common sensors are cross-correlated with one another to identify the lag associated with the highest cross-correlation coefficient for each event pair. It is beneficial to define a minimum cross-correlation coefficient and organize the waveforms into preliminary multiplets so they can



- 3. Calculate the relative locations using hypoDD: Run hypoDD to compute the relative locations of events using Eq. (5).
- 4. *Inspect the results*: Inspect the differential travel-time residuals and location results to ensure they are adequate. While this is subjective, if it does not appear to be correct repeat steps 2–3 and reevaluate.
- 5. Anchor the relative locations to absolute locations for each multiplet: Since hypoDD computes relative locations, a position within each multiplet must be anchored to an absolute location in 3D space. This can be achieved by finding the absolute location of one event, or the centroid of multiple events, for each multiplet using an absolute location method, or some other a priori knowledge of fault location such as a computerized tomography (CT) scan. All the events in each multiplet can then be translated in 3D space so that the absolute location is anchored to its corresponding position while maintaining the relative locations of events in the multiplet.

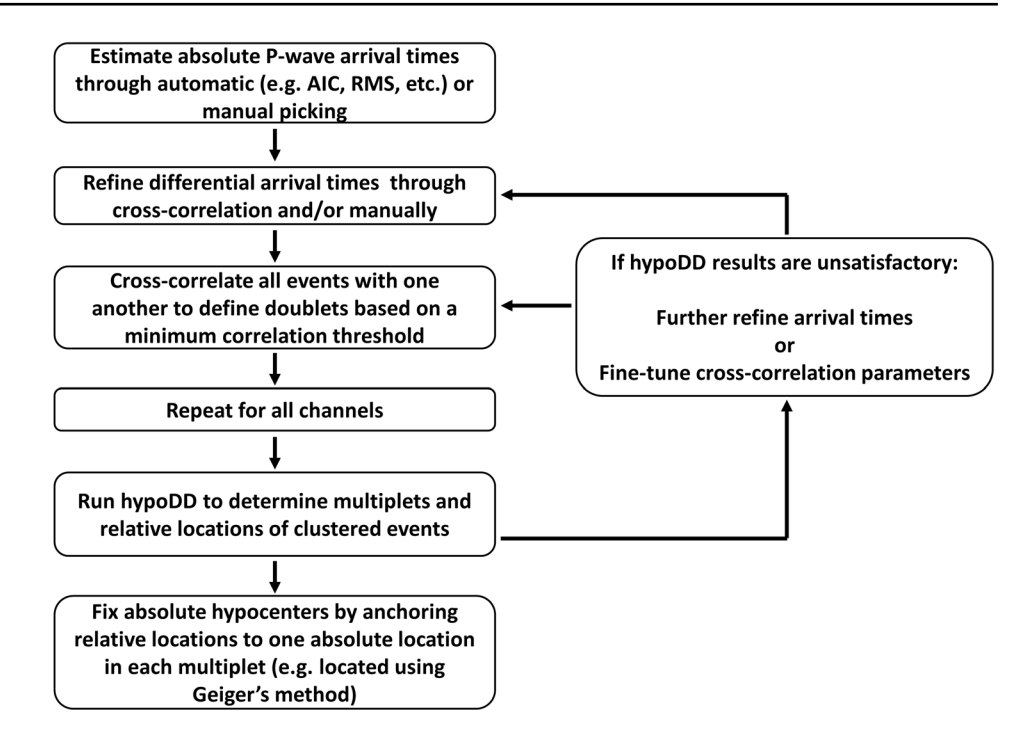
A flow chart detailing the process is shown in Fig. 1.

Experimental methods

Experiments were carried out at beamline 13-BM-D of the Advanced Photon Source (APS), Argonne National Laboratory in the deformation-DIA (D-DIA) module. During isotropic compression, the 250 ton main ram of a hydraulic press controls the advancement of four horizontal and two vertical anvils with squared-off faces with 6 mm edge lengths. The anvils are in contact with a $9 \times 9 \times 8$ mm rectangular prism composed of amorphous boron impregnated with epoxy. Under HPHT, the D-DIA allows for controlled deformation of the sample by the advancement of the top and bottom differential rams which act independently from



Fig. 1 Flow chart detailing the steps required to calculate double-difference relative locations using hypoDD



the main hydraulic ram. For a full description of the D-DIA see Wang et al. (2003). The top, bottom and two of the horizontally situated anvils located on the upstream side of the beam are composed of WC, while the two downstream anvils are composed of sintered diamond (SD) which are transparent to X-rays. A monochromatic synchrotron X-ray beam with 51 keV was used to collect X-ray diffraction patterns and radiographic images for in situ determination of stress and strain respectively. A diagram of the experimental setup is shown in Fig. 2a.

Samples consisted of fully dense polycrystalline "rocks" of olivine structured Mg₂GeO₄ containing ~ 10% MgGeO₃ pyroxene. It has been shown repeatedly that Mg₂GeO₄ undergoes HPHT seismogenic faulting as a result of the HPHT phase transformation from olivine to spinel structure, analogous to the olivine to ringwoodite transformation which is thought to generate deep-focus earthquakes between ~ 350 and 700 km depth (e.g. Green and Burnley 1989; Burnley et al. 1991; Green et al. 1992; Rigg and Green 2005; Shubnel et al. 2013; Wang et al. 2017). The starting sample dimensions were 2.1 mm in diameter and 3 mm long with a grain size that ranged from ~ 50 to 75 μ m. The sample was located at the center of a cylindrical hole traversing the length of the boron epoxy pressure cell. A graphite furnace fitted into the hole generated high temperature through resistive heating. Temperature was determined based on power/ temperature calibrations with an uncertainty of $\sim 10\%$. Inserted on both ends of the sample are 2.5 µm discs of X-ray absorbent Pt foil whose separation defines the sample length in radiographic images. The sample and foil are sandwiched between fully dense 1.3 mm long Al₂O₃ cylindrical pistons used to squeeze the sample and axially deform it when the differential rams are advanced. Beyond the pistons, 1.2 mm long porous Al_2O_3 cylinders are inserted to enclose the pressure cell. During cold compression the ~30% porosity of the porous Al_2O_3 cylinders is reduced to avoid sample fracture at low pressure. A cross-section of the high-pressure cell assembly is shown in Fig. 22b.

Acoustic emission monitoring

AE events were collected by six commercially manufactured piezoelectric lead zirconate titanite (PZT) ultrasonic sensors incorporating a 1/4 wave plate for phase matching and a backing element for damping. They were forced into contact with the rear surface of each anvil using a compressed spring with a thin layer of high-temperature ultrasonic couplant applied between the anvil and sensor face. The front and rear faces of the anvils were polished to a mirror finish to ensure flatness and maximize ultrasonic transmission. The geometry of the anvils/sensors is such they form three opposing sensor pairs orthogonal to one another creating an array (see Fig. 2a). The sensors are sensitive to waves polarized perpendicular to the anvil's rear surface and, in general, can be excited by any acoustic signals with a component of polarization in this direction. This could include P-, S- and surface waves as well as reflected and scattered waves. However, due to the geometry of the apparatus, we expect the vast majority of acoustic energy will be polarized longitudinally. The sensors have a resonant frequency of 2 MHz with a bandwidth ranging from 0.5 to 4 MHz at the -20 dB level.



29 Page 6 of 13 Physics and Chemistry of Minerals (2022) 49:29

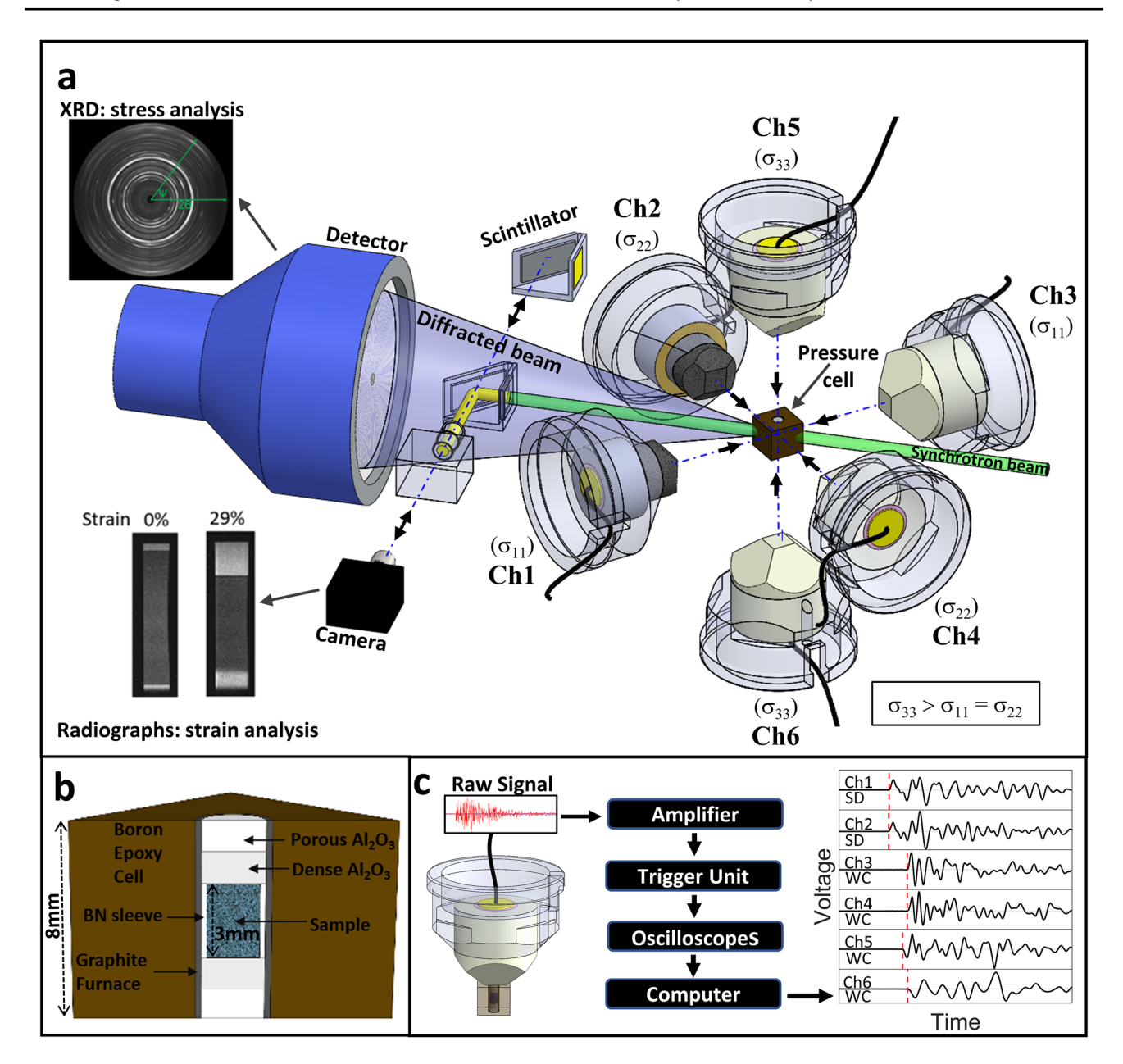


Fig. 2 a Schematic of the experimental setup. The pressure cell is situated at the center of six anvils. The black arrows indicate the advancement of the anvils to contact the cell. Fastened to the rear surfaces of the anvils are piezoelectric sensors. Channels 1 and 2 are fastened to sintered diamond (SD) anvils. Channels 3–6 are fastened to WC. Anvils 5 and 6 are able to advance independent of nvils 1–4. A monochromatic synchrotron beam (green) passes through the pres-

sure cell and is diffracted and measured by the detector for stress measurement. The camera and scintillator move in and out of the beam path (indicated by the double-sided arrows) to capture radiographs of the sample length. $\bf b$ A cross-section of the pressure cell with all components labelled. $\bf c$ A diagram of the acoustic emission system displaying the electronic components and waveforms from a representative event

The manufacturer's frequency response curve is shown in Fig. S1 in Online Resource 1. Each sensor is connected to an amplifier with a flat response covering the sensor bandwidth and saturate at 8 V. Signals were amplified by 40 dB and sent to a trigger and hit count logic control unit that requires signals to overcome a voltage threshold to be recorded. The threshold was set to 75 mV on channels

1–4 and 200 mV on channels 5 and 6, which tend to pick up higher amounts of electrical noise, since they are used for passing electrical current for heating, and their ground connection is in contact with the press and the differential rams. The trigger logic was configured such that waveforms on all six channels would be recorded provided at least two channels crossed the threshold within 50 µs of



one another. Triggered signals were sampled at 50 MHz and transferred to the computer for storage. A data buffer captures 40.96 µs (25%) of the 163.84 µs long trace prior to the first threshold crossing to ensure that the P-wave arrival was recorded on each channel. Figure 2c shows a schematic of the acoustic emission system.

Experimental procedure

Samples were cold compressed (quasi)hydrostatically to 0.2 MN (~3 GPa) over the course of ~6 h to avoid lowpressure fracture. The absence of low-pressure fracture was verified by the lack of AE events recorded in, or near, the sample during this stage of the experiment. Samples were then annealed at high pressure for 45 min at 400 °C, which is below the kinetic boundary required for olivine to transform to spinel. After annealing deformation was commenced with a strain rate of $\sim 5 \times 10^{-5}$ s⁻¹ while keeping the temperature at 400 °C for the first 10% of stain. Here we define strain as the change in length, ΔL , with respect to the initial length, L, along the sample cylindrical axis ($\Delta L/L$). The purpose of this initial low-temperature deformation stage was to build up elastic strain in metastable Mg₂GeO₄ olivine. No AEs were recorded during this stage of deformation. Once 10% strain was reached, the temperature was increased to 700 °C to initiate the transformation to spinel. At this point, large numbers of AEs started to appear and continued for the duration of the experiment. Once the sample reached 32% strain, deformation was stopped and the sample quenched.

3500

3000

2500

2000

1500

1000

500

0

Cumulative Energy (a.u.)

40

Events/min.

10

1000

2000

3000

Time (s)

4000

5000

Fig. 3 Evolution of temperature, stress, strain, AE rate and cumulative AE energy as a function of time during the experiment. The transparent blue box on the right side of the figure indicates the conditions where the transformation from olivine to spinel was promoted. Note that all acoustic activity occurred within this region

(7)where A_i is the amplitude of the waveform's analytical envelope at point j, NF is the length of the front window in P = 3.2 GPaP = 2.5 GPa 800 0.35 2.5 Metastable Olivine + Spinel Olivine 700 0.3 2 600 0.25 0.2 emperature 0.15 300 0.1

200

100

6000

Results

In total, 1456 AE events were recorded during the deformation stage of the experiment, all of which occurred after increasing temperature to 700 °C where transformation to spinel was expected. Figure 3 shows the evolution of temperature, stress, strain, AE rate, and cumulative acoustic energy release as a function of time. Here we define the acoustic energy of an event as the sum of the voltage squared over the first 5 µs after the P-wave phase arrival $(\sum_{t=0}^{5\mu s} V^2)$ averaged over all channels. The waveforms were initially filtered using a 5 MHz low-pass Butterworth filter to remove high-frequency electrical noise from the signals. Since neither the transducers nor the amplifiers used can collect frequencies above ~ 4 MHz, this had a negligible impact on the overall shape of the waveforms. Initial estimates of P-wave arrival times were picked using an RMS amplitude approach which operates by calculating an auto-picking function using a moving window method. At each data point, i, two windows are generated: a front window and a back window. The value of the auto-picking function, F_i , is calculated using the equation,

$$F_{i} = \frac{\sqrt{\sum_{j=i+1}^{i+NF} \left(A_{j}^{2}\right)}}{\sqrt{\sum_{j=i-NB}^{i-1} \left(A_{j}^{2}\right)}}$$
(7)



0.5

0.05

29 Page 8 of 13 Physics and Chemistry of Minerals (2022) 49:29

data points and *NB* is the length of the back window in data points. The auto-picking function represents a difference in the energy contained in the front window compared to the back window. Maxima occur in the function where waveform signals suddenly increase in amplitude relative to data behind it defining the phase arrival. In most cases, arrival times were picked within 1 µs of their true values. For larger discrepancies phase picks were adjusted manually.

Starting with the arrival times discussed above, each waveform was cross-correlated with all others on a common channel using a window length of 6 µs starting 1 µs before the P-wave arrival. A window of this size allowed for ~5 dominant periods to be contained within it. This was initially carried out to refine differential arrival times and center similar waveforms to a constant time lag. Figure 4 shows an example of the time lags for some similar waveforms before and after cross-correlation that demonstrate the effectiveness of the approach. Prior to cross-correlation the time lags between waveforms differ by as much as $\sim 0.7 \,\mu s$ which is longer than the time it takes for the waveforms to traverse the sample. However, after correlation-based adjustment they become essentially identical. To visualize the degree of correlation on each channel an $N \times N$ symmetric matrix was created, where N is the total number of events, with each element, $C_{ii} = C_{ii}$, representing the maximum value computed by cross-correlation of events i and j. The diagonal elements are equal to unity as they represent auotcorrelation. Crosscorrelation matrices for each channel are shown in Fig. 5. Note that the degree of correlation differs substantially on

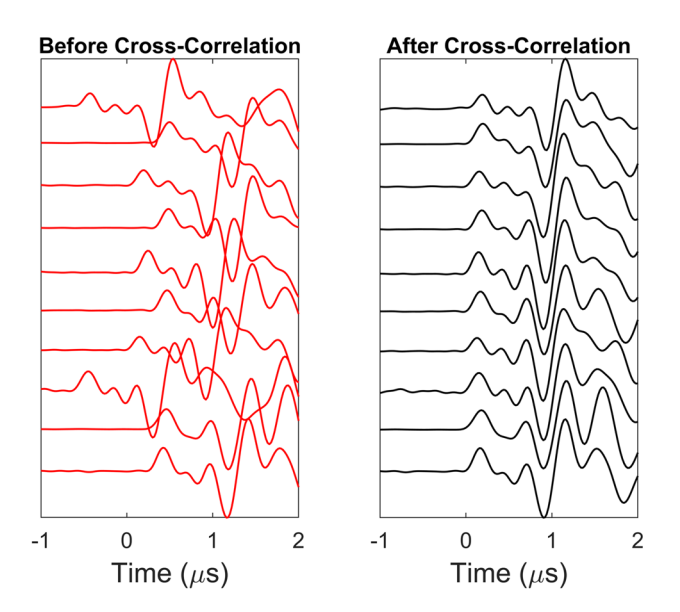
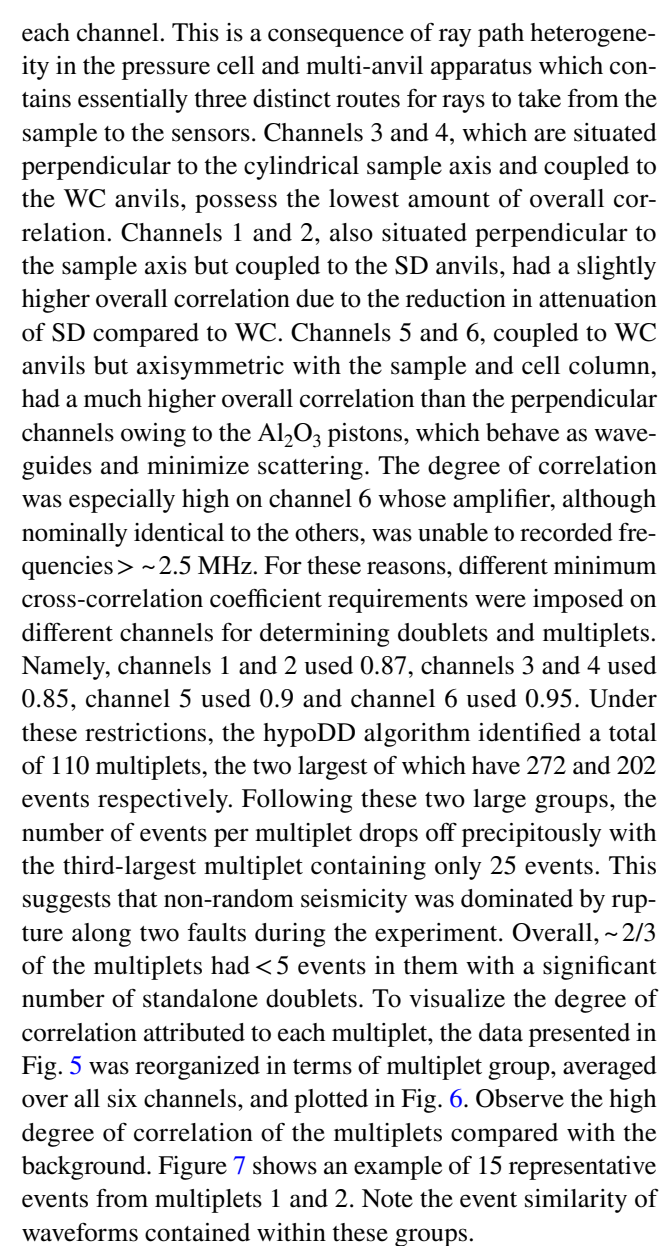


Fig. 4 An Example of P-wave phase picking refinement for 10 similar AE events recorded on channel 1. The figure on the left shows the time lags of event picked using the RMS amplitude method before cross-correlation. The figure on the right shows the same waveforms aligned to a common phase lag after cross-correlation



In addition to establishing the multiplet connectivity, hypoDD also determines the relative locations of events within each multiplet using the double-difference method. Since hypoDD relies on relative arrival times and we expect events within a multiplet to be clustered within a restricted volume, velocity heterogeneities resulting from the anvils and pressure cell cancel out. Subsequently, only the P-wave velocity of the sample is required to fully define the velocity model. At ambient conditions, the P-wave velocity of Mg₂GeO₄ is 7.32 m/s (Weidner and Hamaya 1983). While we do not know the precise P-wave velocity of the sample under our experimental conditions, the application of pressure and temperature serve to increase and decrease the P-wave velocity, respectively, so these competing effects tend to cancel each other out to some degree. The effect of the velocity imprecision functions to inflate/deflate the overall volume of



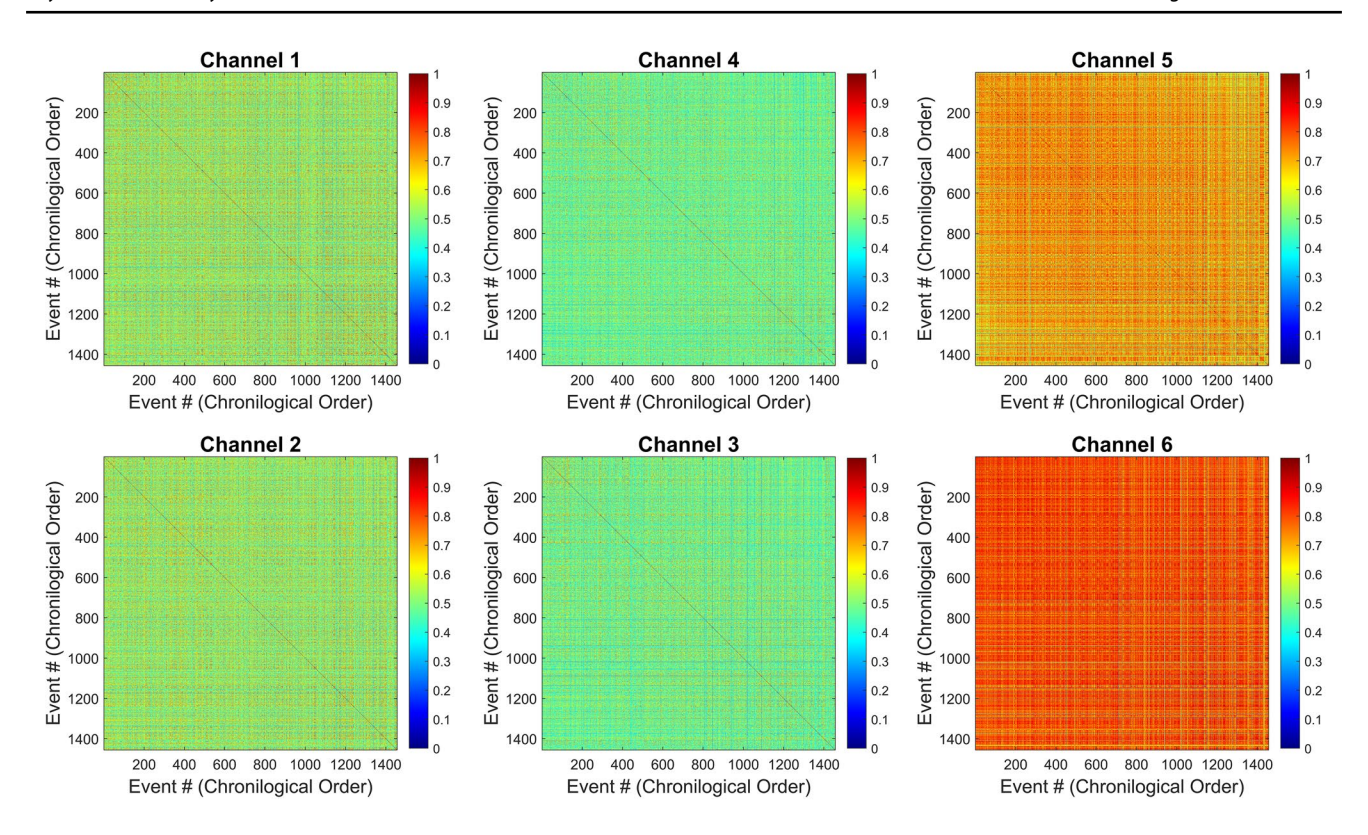


Fig. 5 Cross-correlation matrices of all 1456 events on all six channels using a 6 μ s time window beginning 1 μ s before the P-wave arrival. The x and y axes represent the event number ordered chronologically. Each entry represents the maximum cross-correlation coefficient of the correlation function. Warmer colors indicate a higher correlation. The matrices are symmetric and the diagonal elements

are equal to unity reflecting autocorrelation. There does not appear to be any chronological pattern of events, indicating primarily random acoustic activity. The degree of waveform correlation varies significantly between channels. Channels 5, and particularly 6, show a very high degree of overall correlation compared to channels 1–4

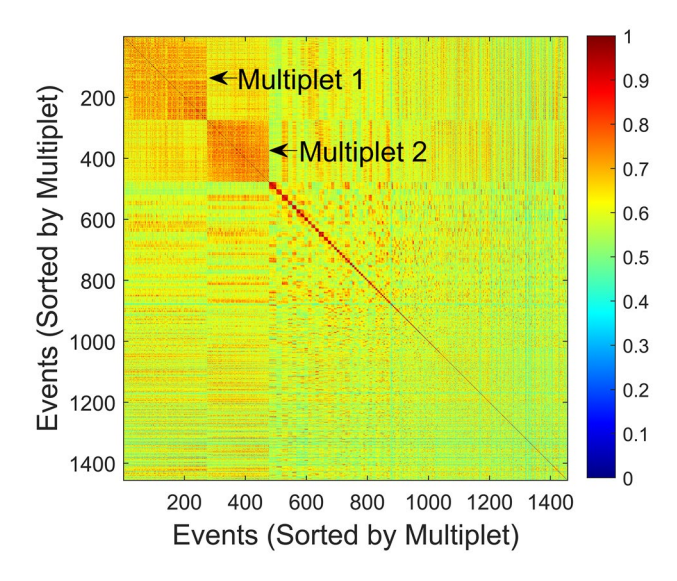


Fig. 6 Maximum cross-correlation values sorted by multiplet group. The first 272 entries belong to multiplet 1. The next 202 entries belong to multiplet 2. Smaller multiplets can be seen descending in size as the entries increase. The last 418 entries do not form doublets and are ordered chronologically

the event cloud, but we expect this contribution to be minimal. Using this velocity and the differential arrival times as inputs we ran the modified hypoDD algorithm, weighted by the cross-correlation coefficients between doublets, to calculate the relative locations of events. Setting the initial solution to the center of the sample and the travel time from the center of the sample to a sensor, Eq. (3) was solved iteratively until the perturbations in location and time were < 1 mm and < 1 ns respectively. Solutions typically converged in < 5 iterations. Solutions consisting of ≤ 4 sensors, and whose relative location was greater than the final sample length, were discarded. To examine the quality of the relative location results, we compared them to absolute locations of the same events computed using Geiger's method (Geiger 1912) with an isotropic velocity model. To ensure the most accurate absolute locations possible, the absolute arrival times of events were picked manually which tends to outperform automatic picking techniques. To account for the increased P-wave velocity in the SD anvils compared to WC, the sensor locations of the sensors coupled to the SD anvils were artificially moved nearer to the sample center in Geiger's algorithm. To estimate the absolute location of the event cloud, it was translated to



29 Page 10 of 13 Physics and Chemistry of Minerals (2022) 49:29

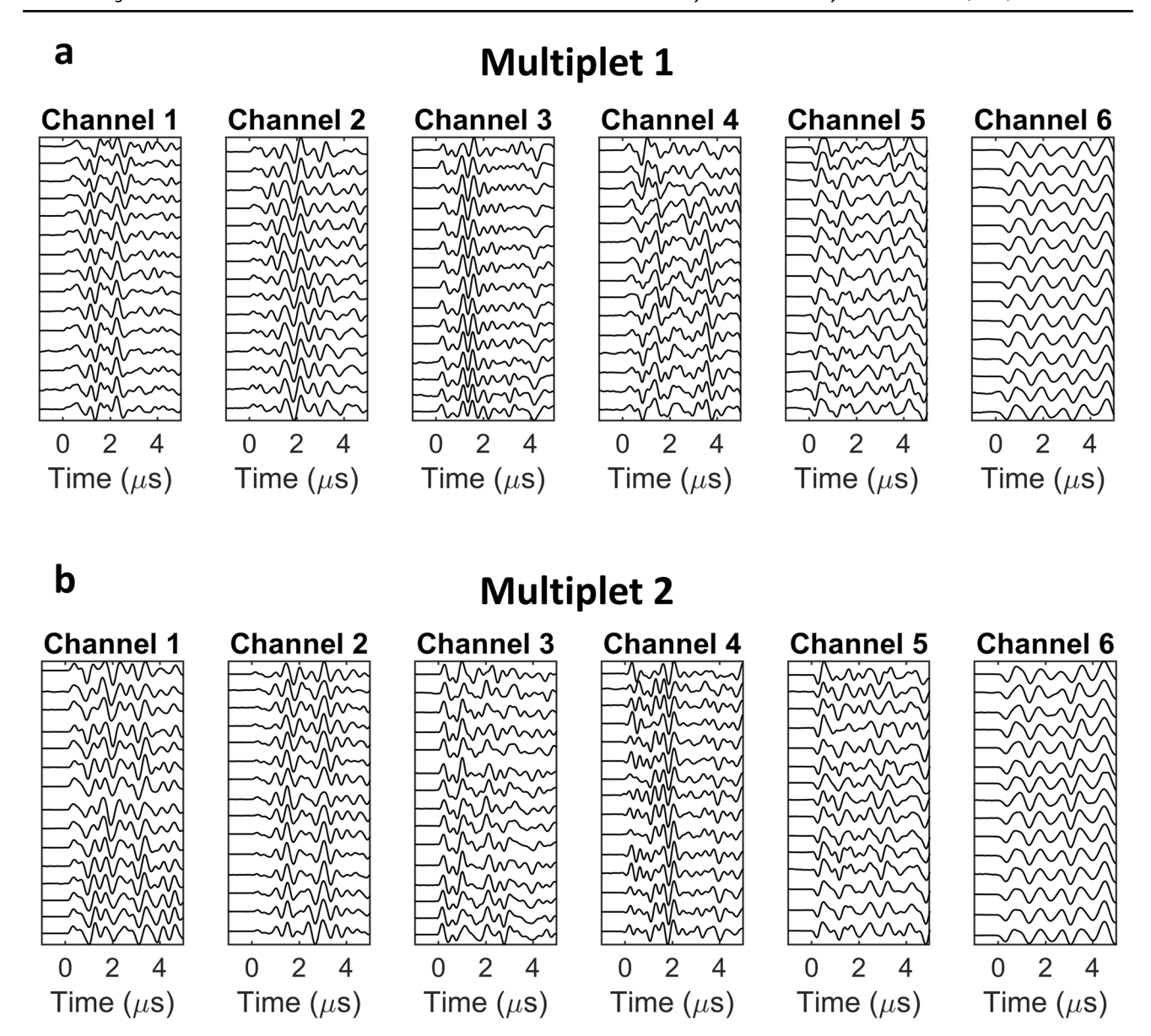


Fig. 7 Example of waveforms from AE events from multiplet 1 (a) and multiplet 2 (b). Waveforms from channel 6, whose amplifier was unable to record frequencies > 2.5 MHz shows a particularly high waveform correlation compared to the other channels

an absolute position by first inspecting the absolute locations of a few events emphasizing a high degree of connectivity to other events in the multipletand a high signal-to-noise ratio. This provided a crude estimate of each multiplet's vicinity. The overall shape of each multiplet was then compared with a CT scan of the recovered sample and their centroids were manually adjusted to coincide with the image. Figure 8a,b compare the relative vs absolute event locations for multiplets 1 and 2 plotted at an oblique angle and projected onto the *x*–*y* plane respectively. It is clear from these images that the application of the double-difference method collapses the volume of clusters considerably. This can also be seen from the dramatic reduction in event separation between each event

pair which is displayed as histograms for multiplets 1 and 2 in Fig. 8c,d respectively. Event location errors were calculated for both the absolute and relative locations of multiplets 1 and 2. For absolute location methods, Pavlis (1986) noted that the source location uncertainty is composed of a combination of three factors: (1) measurement error, (2) velocity model error and (3) non-linear terms. In the case of relative location methods, a fourth factor related to interactions of errors caused by variation in the number and quality of events can also play a role (Pavlis 1992). In our analysis, we have only considered measurement error and neglected the other factors whose contributions are difficult to estimate. The standard deviation of data was estimated using the RMS of travel-time residuals



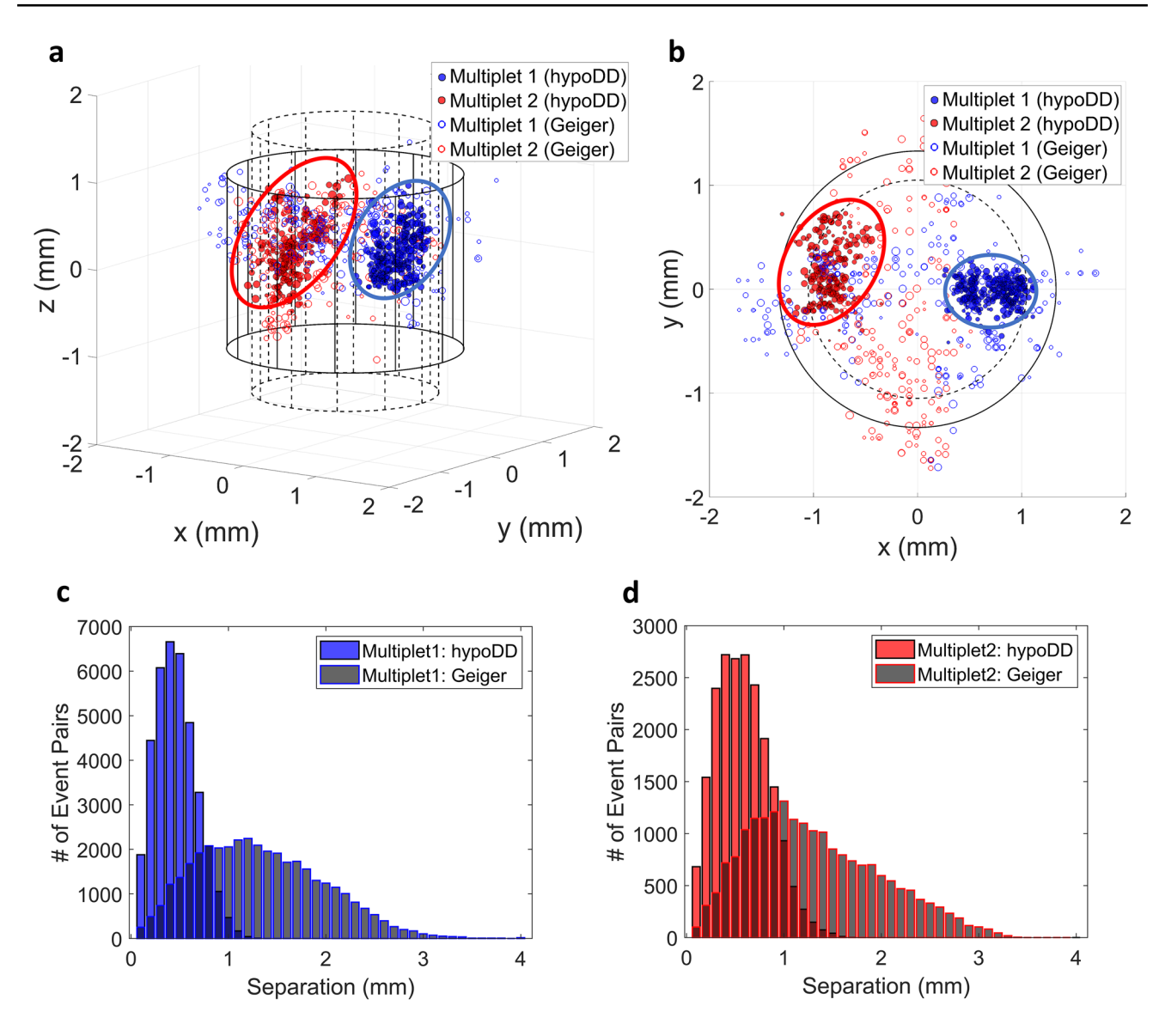


Fig. 8 a Obliquely plotted view of the relative event locations computed using hypoDD for multiplets 1 (solid blue circles) and 2 (solid red circles) compared to the absolute locations of multiplets 1 (open blue circles) and 2 (open red circles) calculated using Geiger's method. The red and blue ellipses bound the event cloud of multiplets 1 and 2 respectively. **b** The same relative and absolute event locations

as shown in **a** projected onto the x–y plane. **c** Histogram comparing event location separation for all event pairs in multiplet 1 for hypoDD (blue) and Geiger's method (grey). **d** Histogram comparing event location separation for all event pairs in multiplet 2 for hypoDD (red) and Geiger's method (grey)

computed in the final iteration. In this sense, our calculated uncertainties are likely lower than in actuality for both the absolute and relative location estimates, however, it provides a basis to make a comparison between errors associated with the two methods. The absolute location uncertainties were calculated to be 0.37 mm and 0.42 mm for multiplets 1 and 2 respectively, compared to 0.01 mm for the double-difference method. While this analysis represents a lower bound on error estimates for both techniques, it is reasonable to assume that the double-difference method increases location accuracy by an order of magnitude. To compare the double-difference

event locations to the position of macroscopic faulting in the sample, the recovered sample was CT scanned. Since the fault represents a region of nearly homogeneous X-ray absorption, an isosurface was generated along the fault surface. Figure 9a shows an image of the reconstructed CT volume with the contrast, transparency and color adjusted to emphasize the presence of the fault. The isosurface was then digitized and plotted together with the double-difference locations. Figure 9b,c show the event locations relative to the fault geometry viewed obliquely and projected onto the *x*–*y* plane respectively. Note that the event locations coincide with both the position and



29 Page 12 of 13 Physics and Chemistry of Minerals (2022) 49:29

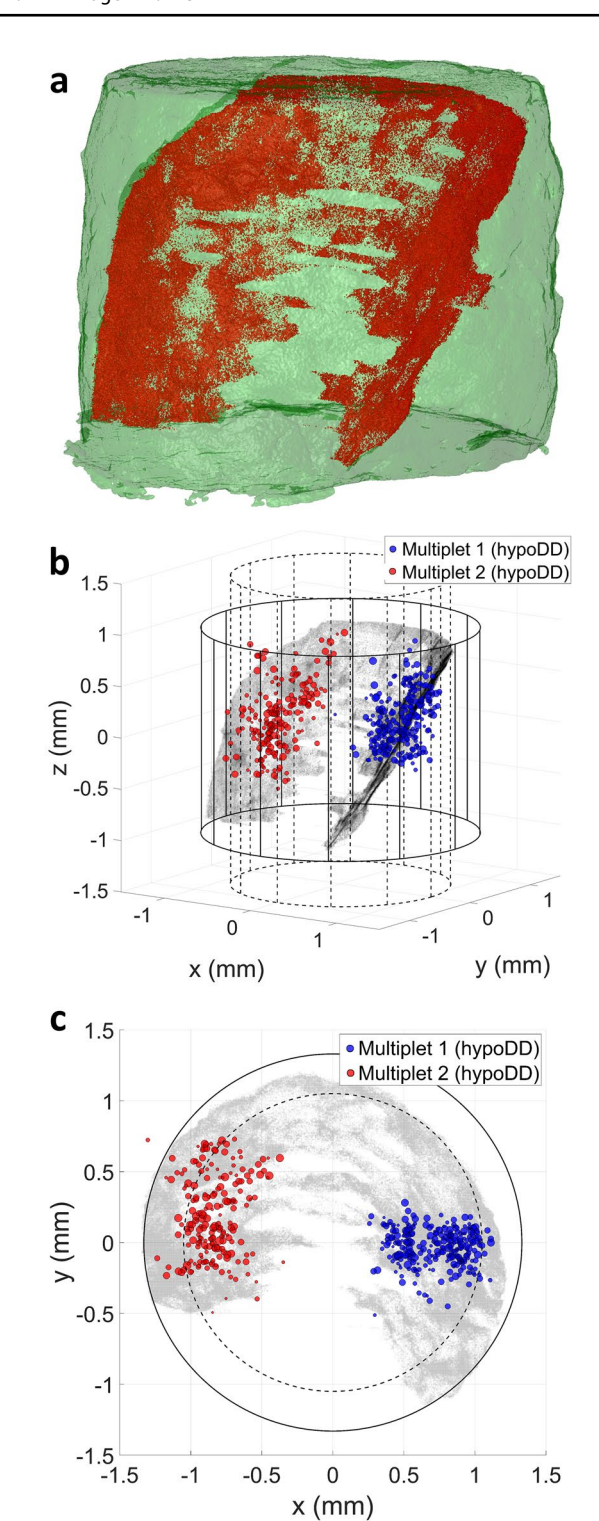
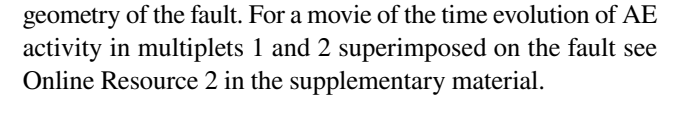


Fig. 9 a CT image of the recovered sample showing a large fault (red) contained within the sample (transparent green). **b** The distribution of event locations from multiplets 1 (blue dots) and 2 (red dots) with respect to a digitized representation of the fault (grey). **c** Top view of the event locations for multiplets 1 and 2 with respect to the digitized fault. In **b,c**, dashed and solid black lines represent the respective sample volume before and after deformation



Discussion and conclusions

The precision of AE event locations in samples contained within the multi-anvil apparatus is affected primarily by two factors: the velocity model used and the accuracy of arrival time picks. In most cases, studies have relied on a homogeneous velocity model and automatic P-wave arrival time picks resulting in location uncertainties of ~0.5 mm. Due to the inherent volume restriction imposed by high-pressure generation, an uncertainty of this size represents a significant proportion of the sample dimensions. This limitation makes it very difficult, if not impossible, to associate specific AE events with the underlying fault structure. Furthermore, most of the acoustic activity takes place randomly in space and time creating a dense cloud of unrelated events that obscures any underlying structures that may be present. For example, in this study, only $\sim 2/3$ of events form doublets, the majority of which belong to multiplets that contain only a handful of events. This indicates that a significant proportion of the acoustic activity is either unrelated to macroscopic failure, or functions primarily in a precursory manner to weaken the sample's integrity and prepare it for macro-fracture. Without the use of cross-correlation it would not be possible to determine faultassociated AE activity since the uncorrelated events would tend to overshadow the presence of event clustering. It is clear from Fig. 8 that the application of the double-difference method significantly reduces the volumes of event clouds compared to absolute location methods. Given that the arrival times used for the absolute locations were picked manually, it is reasonable to assume that they are accurate to ~ 1 or 2 data points (20–40 ns). Therefore, it seems unlikely that absolute location methods would be able to be used to delineate specific faults without employing a more complex velocity model. However, given the uncertainty of P-wave velocities under in situ conditions of HPHT for the wide variety of materials used in multi-anvil experiments, it will likely prove challenging to readily resolve this issue. For this reason, double-difference location methods, which essentially remove the effect of velocity heterogeneities, provide the most straightforward means of accurately locating events. Nevertheless, because double-difference methods only provide relative event locations, one position within each cluster must still be anchored to a specific location. One of the advantages of simulating deep-focus earthquakes in the laboratory is that we have direct access to the location and geometry of faults generated in our experiments through non-destructive CT imaging of the recovered sample. This allows us to explicitly relate AE event locations with visually observed faults, a luxury not afforded to earthquake seismologists. While the two



largest multiplets form event clusters associated with faulting on opposite sides of the sample (Fig. 9), reducing the correlation coefficient by ~0.05 merges both multiplets into a single multiplet, suggesting the two clusters are manifestations of two distinct subfaults on a single larger fault which is seen to connect near the top of the CT image (Fig. 9a). This suggests that in future studies it may be possible to reconstruct spatiotemporal rupture complexity in HPHT experiments and follow the faulting process from nucleation to rupture initiation and subsequent slip.

Supplementary Information The online version contains supplementary material available at https://doi.org/10.1007/s00269-022-01203-8.

Acknowledgements We acknowledge the National Science Foundation (Grant Nos. EAR-1661489, EAR-1661519 and EAR-1925920) for providing funding for this research. We would also like to acknowledge GeoSoilEnviroCARS (The University of Chicago, Sector 13), Advanced Photon Source (APS), Argonne National Laboratory where the experiments performed.

Declarations

Conflict of interest The authors declare no conflicts of interest.

References

- Akaike H (1974) Markovian representation of stochastic processes and its application to the analysis of autoregressive moving average process. Ann Inst Stat Math 26:363-387
- Allen R (1982) Automatic phase pickers: their present use and future prospects. Bull Seismol Soc Am 72:225-242
- Anant KS, Dowla FU (1997) Wavelet transform methods for phase identification in three-component seismograms. Bull Seismol Soc Am 87:1598-1612
- Arrowsmith SJ, Eisner L (2006) A technique for identifying microseismic multiplets and application to the Valhall field, North Sea. Geophysics 71:V31–V40
- Burnley PC, Green HW, Prior DJ (1991) Faulting associated with the olivine to spinel transformation in Mg₂GeO₄ and its implication for deep-focus earthquakes. J Geophys Res 96:425-443
- Cano EV, Akram J, Peter DB (2021) Automatic seismic phase picking based on unsupervised machine-learning classification and content information analysis. Geophysics 86:V2999-V3315
- Castellanos F, van der Bann M (2013) Microseismic event locations using the double-difference algorithm. CSEG Rec 38:26-37
- De Meersman K, Kendall J-M, van der Baan M (2009) The 1998 Valhall microseismic data set: an integrated study of relocated sources, seismic multiplets, and S-wave splitting. Geophysics 74:B183-B195
- de Ronde AA, Dobson DP, Meredith PG, Boon SA (2007) Threedimensional location and waveform analysis of microseismicity in multi-anvil experiments. Geophys J Int 171:1282-1294
- Frohlich C (2006) Deep Earthquakes. Cambridge University Press Geiger L (1912) Probability method for the determination of earthquake epicenters from the arrival time only (translated from Gei-
- ger's 1910 German article). Bull St Louis Univ 8(1):56-71 Geller RJ, Mueller CS (1980) Four similar earthquakes in central California. Geophys Res Lett 7:821-824

- Got J-L, Frechet J, Klein FW (1994) Deep fault plane geometry inferred from multiplet relative relocation beneath the south flank of Kilauea. J Geophys Res 99:15375-15386
- Green HW, Burnley PC (1989) A new self-organizing mechanism for deep-focus earthquakes. Nature 341:733-737
- Green HW, Scholz CH, Tingle TN, Young TE, Koczynski TA (1992) Acoustic emissions produced by anticrack faulting during the olivine to spinel transformation. Geophys Res Lett 19:789-792
- Li Z, Zhu L, Officer T, Shi F, Yu T, Wang Y (2022) A machinelearning-based method of detecting and picking the first P-wave arrivals of acoustic emission events in laboratory experiments. Geophys J Int 230:1818-1823
- Mousavi SM, Ellsworth WL, Zhu W, Chuang LY, Beroza GC (2020) Earthquake transformer—an attentive deep-learning model for simultaneous earthquake detection and phase picking. Nat Commun 11:3952
- Pavlis GL (1986) Appraising earthquake hypocenter location errors: a complete, practical approach for single-event locations. Bull Seismol Soc Am 76:1699-1717
- Pavlis GL (1992) Appraising relative earthquake location errors. Bull Seismol Soc Am 82:836-859
- Officer T, Secco RA (2020) Detection of high P, T transformational faulting in Fe2SiO4 via in-situ acoustic emission: Relevance to deep-focus earthquakes. Phys Earth Planet Int 300:106429
- Ohuchi T, Lei X, Higo Y, Tange Y, Sakai T, Fujino K (2018) Semi-brittle behavior of wet olivine aggregates: the role of aqueous fluid in faulting at upper mantle pressures. Contrib Mineral Petrol 173:88
- Riggs EM, Green HW (2005) A new class of microstructures which lead to transformation-induced faulting in magnesium germinate. J Geophys Res 110:B03202
- Ross ZE, Meier M-A, Hauksson E (2018) P wave arrival picking and first-motion polarity determination with deep learning. J Geophys Res Solid Earth 123:5120-5129
- Saad OM, Chen Y (2021) Earthquake detection and P-wave arrival time picking using capsule neural network. IEEE Trans Geosci Remote Sens 99:6234-6243
- Shi F, Wang Y, Yu T, Zhu L, Zhang J, Wen J, Gasc J, Incel S, Schubnel A, Li Z, Chen T, Liu W, Prakapenka V, Jin Z (2018) Lower-crustal earthquakes in southern Tibet are linked to eclogitization of dry metastable granulite. Nat Commun 9:3483
- Shubnel A, Brunet F, Hilariet N, Gasc J, Wang Y, Green HW (2013) Deep-focus earthquake analogs recorded at high pressure and temperature in the laboratory. Science 341:1377-1380
- Sleeman R, van Eck T (1999) Robust automatic P-phase picking: An on-line implementation in the analysis of broad-band seismogram recording. Phys Earth Planet Inter 113:265-275
- Wadati K (1927) Existence and study of deep earthquakes (in Japanese). Meteorol Soc Jpn Ser II 5:119-145
- Waldhauser F, Ellsworth WL (2000) A double-difference earthquake location algorithm: method and application to the northern Hayward fault, California. Bull Seismol Soc Am 90:1353-1368
- Wang Y, Durham WB, Getting IC, Weidner DJ (2003) The deformation-DIA: A new apparatus for high temperature triaxial deformation to pressures up to 15 GPa. Rev Sci Instrum 74:3002-3011
- Wang Y, Zhu L, Shi F, Schubnel A, Hilariet N, Yu T, Rivers M, Gasc J, Addad A, Deldicque D, Li Z, Brunet F (2017) A laboratory nanoseismological study on deep-focus earthquake micromechanics. Sci Adv 3:1-12
- Weidner DJ, Hamaya N (1983) Elastic properties of the olvine and spinel polymorphs of Mg₂GeO₄, and the evaluation of elastic analogues. Phys Earth Planet Int 33:275–283

Publisher's Note Springer Nature remains neutral with regard to jurisdictional claims in published maps and institutional affiliations.

